



NaCl-Induced High-Temperature Corrosion of Alloy 625 Fabricated by Laser Metal Deposition-Powder

Agathe Curnis^{1,2} · Ioana Popa² · Aurélien Prillieux¹ · Jean-Michel Brossard³ · Sébastien Chevalier²

Received: 11 July 2024 / Revised: 11 July 2024 / Accepted: 20 July 2024

© The Author(s), under exclusive licence to Springer Science+Business Media, LLC, part of Springer Nature 2024

Abstract

The present study describes the corrosion behavior of alloy 625 fabricated by laser metal deposition-*powder* in the presence of a solid NaCl deposit in laboratory air at 650 and 800 °C. The results showed that at both temperatures, the presence of the deposit had a catastrophic effect on the corrosion resistance of the alloy. The active corrosion mechanism resulted in a very thick and non-protective oxide scale and in a highly damaged metal zone beneath the oxide scale. Although the mechanism involved was the active corrosion mechanism at both 650 and 800 °C, differences were observed between these two temperatures. At 800 °C, the corrosion products were thicker, and the substrate was significantly more damaged, especially due to the formation of an interconnected network of voids. At 650 °C, the thick and continuous Cr₂O₃ layer, predominantly observed at 800 °C, was not present. The use of thermodynamic data helped to suggest possible explanations for the observed differences. Overall, the increase of temperature accelerated the degradation of the alloy and it was enhanced by a radical change of the main reactions of the active corrosion mechanism between 650 and 800 °C.

Keywords Additive manufacturing · Ni-based alloy · High-temperature corrosion · NaCl solid deposit

Introduction

Additive manufacturing provides new perspectives in terms of engineering and materials. If the additive manufacturing (AM) offers the possibility to fabricate parts with complex geometries and to reduce the number of assembly steps, it also generates specific microstructures that lead to unique properties. However, several studies revealed differences in the behavior of materials produced by AM and those

Extended author information available on the last page of the article

produced by conventional processes, supporting the idea that further researches on additively manufactured materials are required [1]. Alloy 625 is particularly well suited for additive manufacturing processes thanks to its excellent weldability. This alloy is particularly used in applications requiring mechanical and corrosion resistance properties, such as aerospace, marine, aeronautics, chemical and petrochemical industries [2–4]. Corrosion resistance of alloy 625 is mainly due to the formation of a Cr_2O_3 layer that enables the alloy to resist to high temperatures, up to 1000 °C [5–7].

Nevertheless, alloy 625 can be exposed to various types of corrosive species during its high-temperature service, particularly in waste-to-energy plant environments or in aeronautical components. In these applications, alloy 625 has to withstand exposure to highly corrosive gases that may contain carbon, sulfur (SO_2 , SO_3), oxygen, chlorine (Cl_2 , HCl), water vapor, but also the presence of solid impurities that may form alkaline chlorides and/or sulfates and heavy metals (Na, K, Zn, Sn) [8]. The presence of chlorinated and/or chloride species in the environment, whether in gaseous form (Cl_2 or HCl) or in solid form combined with other elements, as alkali or metal chlorides (NaCl , KCl , ZnCl_2 , PbCl_2), prevents the formation of protective oxide scales and accelerates material degradation [9]. The active corrosion mechanism is generally used to explain the alloy degradation when a chlorinated specie is present in the environment [10–13]. This mechanism involves several steps. The first step is the formation of gaseous chlorine, according to various reactions [8, 11, 14]. Then, gaseous chlorine migrates through the oxide scale to the metal substrate. At the metal/oxide interface, the oxygen partial pressure is very low and thus favors the reaction between gaseous chlorine and the metallic elements in the substrate. These reactions between metallic elements and gaseous chlorine result in the formation of metal chlorides. At high temperatures and low oxygen partial pressures, the metal chlorides formed are highly volatile and diffuse outward through the oxide scale. As they migrate toward the surface, the oxygen partial pressure increases until reaching the value where the corresponding metal oxide is thermodynamically more stable than the chloride. Then, the formation of the oxide releases gaseous chlorine in the system which will be used to reproduce the cycle described above, leading to a self-sustained mechanism.

The active corrosion mechanism leads to the formation of thick, damaged and non-protective oxide scales and can also result in the deterioration of the subsurface metal zone [9, 15–18]. At 650 °C, Wang et al. [19] evaluated the corrosion behavior of alloy 625 exposed to 50 wt.% KCl + 50 wt.% NaCl deposit. The authors reported two substructures in the resulting oxide layer: a NiO layer at the outer part and a Cr-rich layer with traces of Nb at the inner part. For alloy 718 with 2 mg cm^{-2} of NaCl deposit exposed at 700 °C, Wu et al. [20], reported the formation of an oxide scale made of two sublayers. The inner sublayer is compact and mainly composed of Cr oxide, while the outer sublayer is more porous and made of spinel oxides containing Ni, Nb and Fe. Zahs et al. [9] observed NiO and Fe_2O_3 in the outer part and Cr_2O_3 in the inner part of the oxide scale of alloy 600 exposed to 600 °C under $\text{N}_2 + 5 \text{ vol}\% \text{ O}_2 + 1500 \text{ vppm HCl}$.

Bender and Schütze [21] demonstrated the detrimental effect of increasing Cl_2 partial pressure on the corrosion resistance of several chromia-forming steels and nickel

alloys, including alloy 625. For instance, when exposed to 800 °C in air containing 2 vol.% Cl₂, alloy 625 exhibited a thick and non-protective oxide layer consisting of Cr₂O₃ in the inner part and a mixed Cr–Fe–Ni oxide in the outer part. These authors also observed the presence of voids and significant Cr depletion of the subscale matrix on thicknesses that are increasing when temperature increases up to 1000 °C.

The aim of the present study is to investigate the influence of a solid NaCl deposit on the high-temperature oxidation behavior in air of alloy 625 produced by laser metal deposition-*powder* and also to evaluate the effect of the temperature on degradation mechanisms.

Experimental Procedures

Deposits of alloy 625 were additively manufactured on a low alloy steel substrate by using the laser metal deposition-*powder* (LMD-*p*) process. A Beam Modulo 400 machine was used, and deposits were produced under protective atmosphere. Spherical gas-atomized alloy 625 powders with particle size distribution of 45–106 μm supplied by Oerlikon were used for additive manufacturing. The chemical composition of the alloy 625 powder, as provided by the supplier, is listed in Table 1. The substrate was an ASTM A387 Grade 22 Class 2 steel plate (100 mm×100 mm×10 mm). Before deposition, the substrate surface was ground and cleaned with acetone to remove the native oxide scale and to improve laser absorptivity.

LMD-*p* parts consisted of 4 successive layers of alloy 625 for a total thickness of 5 mm. For corrosion experiments, squared samples with a side length of 10 mm were cut by electrical discharge machining from the additively manufactured parts. The specimens were mechanically ground on SiC abrasive papers up to P600 grade and ultrasonically cleaned with ethanol.

Corrosion tests were performed at 650 and 800 °C in laboratory air with NaCl solid deposits on the additively manufactured alloy 625 in the as-built state. The protocol used to produce the 3–4 mg cm⁻² NaCl deposits (corresponding to a deposit covering around 75–85% of the sample surface), and the corrosion tests were already described in a previous paper [22]. Specimens were exposed up to 5000 h at 650 °C and up to 2500 h at 800 °C.

The surfaces of all samples were characterized by SEM and XRD before performing SEM observations on cross sections. The samples preparation the characterization technics and the associated conditions were described previously [22].

Thermodynamics calculations were performed with FactSage 6.4 using reaction module and FactPS/FT Oxid and FTSalt databases.

Table 1 Chemical composition of alloy 625 powder (in wt.%)

Elements	Ni	Fe	Cr	Mo	Nb	Si	Mn	C
Alloy 625 powder	Bal	1.7	21.5	9.5	4	0.4	0.4	0.01

Results

Figure 1 shows the SEM surface images of alloy 625 samples with solid NaCl deposit after exposure at 650 and 800 °C. These images reveal that, at both temperatures, the oxide scale is non-homogeneous and severely damaged. Cracks, blisters and spallation are visible. Spallation occurred especially at 800 °C. The complete spallation of the oxide scale in localized areas of the sample, as observed in Fig. 1c, reveals the presence of numerous voids at the metal/oxide interface.

After exposure at 800 °C, the XRD pattern shows the presence of a face-centered cubic phase in the oxide scale. According to SEM–EDS analyses, this phase was identified as NiO. A rhombohedral Cr₂O₃ phase was also present, in agreement with SEM–EDS analyses, in regions where the oxide scale is partially spalled. In addition to these two phases, a spinel oxide phase was identified by XRD. According to SEM–EDS surface analyses, in addition to Ni and Cr, some Fe and Nb are also present in intermediate location in the oxide scale. At 650 °C, the results of XRD and SEM–EDS surface analyses indicate the presence of the same three oxide phases (NiO, spinel and Cr₂O₃). However, with the same analysis parameters, the relative intensities of the diffraction peaks of the three phases are different from those obtained at 800 °C.

The SEM cross-section images in Fig. 2 show the evolution of the oxide scale with the exposure time at 650 and 800 °C. At both temperatures, the oxide scales are strongly damaged, in agreement with the surface observations, and their thicknesses increase in time. At 800 °C, in addition to the thick oxide scale, the metal beneath is highly damaged. Findings of a previous investigation on these samples show that an interconnected voids network is present in this region of the substrate [22]. At 650 °C, the oxide scale is composed of two major parts: an inner part, which is relatively dense and compact, and an outer part that forms porous domes.

The SEM images presented in Fig. 2 allow the comparison of the oxide scales formed at the two studied temperatures, 650 and 800 °C. The thicknesses of the oxide scales are listed in Table 2. Note that at 800 °C the thickness may be underestimated due to spalling. At 650 °C, the thickness of the compact oxide scale located in the inner part of the corrosion scale is also given. Indeed, due to the presence of the domes, the total thickness of the oxide scale is heterogeneous and significantly evolves over the width of the sample.

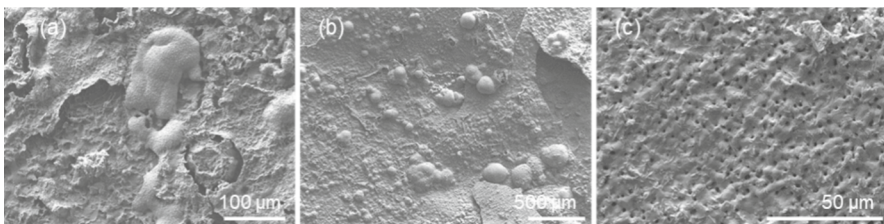


Fig. 1 Surface SEM images of LMD-*p* alloy 625 samples with NaCl solid deposit aged in laboratory air for 100 h at **a** 650 °C and **b**, **c** 800 °C

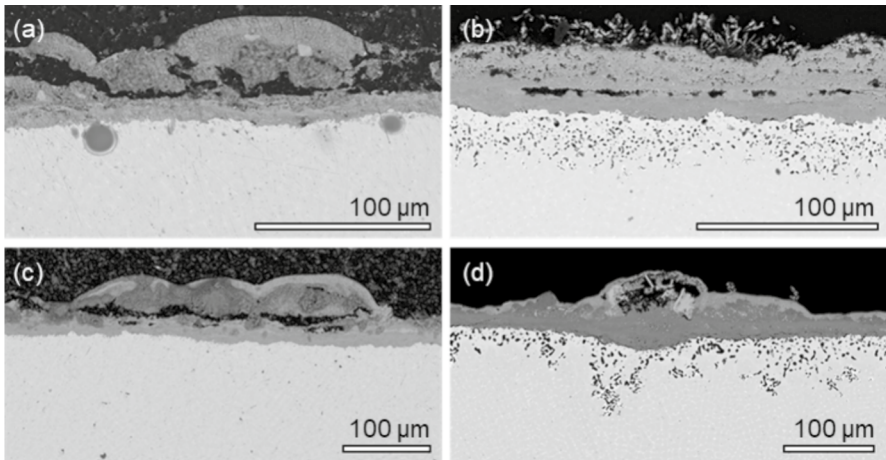


Fig. 2 Cross-section SEM images of LMD-*p* alloy 625 samples with NaCl solid deposit aged in laboratory air for: **a** 24 h at 650 °C, **b** 24 h at 800 °C, **c** 500 h at 650 °C and **d** 500 h at 800 °C

Table 2 Oxide scale thickness (in μm) depending on temperature and exposure time (error is twice the standard deviation). Values given for 24 h and 1000 h at 800 °C are extracted from a previous work [22]

	24 h	500 h	1000 h	5000 h
650 °C	24.0 ± 9.8	30.6 ± 16.4	47.8 ± 21.2	61.8 ± 21.9
(inner part)	(11.4 ± 1.4)	(15.9 ± 4.2)	(17.2 ± 6.8)	(24.0 ± 5.9)
800 °C	19.9 ± 7.5	42.6 ± 14.2	82.7 ± 27.5	–

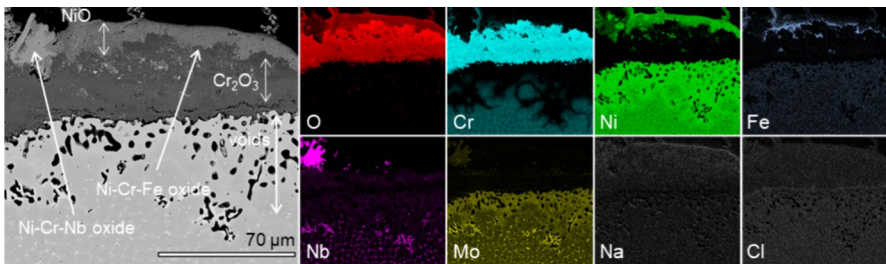


Fig. 3 Cross-section SEM image of LMD-*p* alloy 625 sample with NaCl deposit aged in laboratory air for 500 h at 800 °C and corresponding X-ray maps

The images in Fig. 3 and Fig. 4 show SEM cross-section observations of alloy 625 samples with solid NaCl deposit after 5000 h and 500 h of exposure at 650 and 800 °C, respectively. The corrosion product compositions are generally similar for both temperatures: The outer part of the scale consists of Ni-rich oxides, while the inner part contains Cr-oxides. At 800 °C, the outer part of the layer is composed of NiO, as identified by surface analyses. The inner part

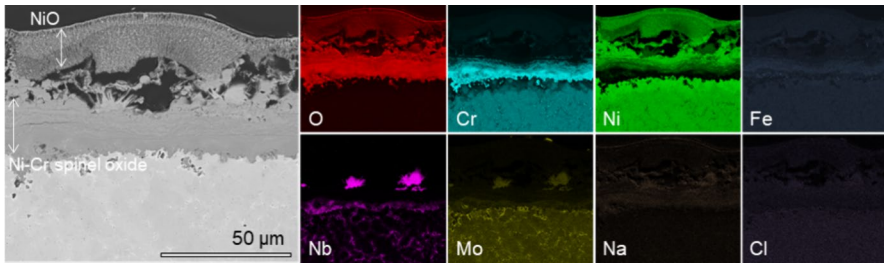


Fig. 4 Cross-section SEM image of LMD-palloy 625 sample with NaCl deposit aged in laboratory air for 5000 h at 650 °C and corresponding X-ray maps

is made of Cr_2O_3 which represents the largest part of the oxide scale. A Ni–Cr oxide, containing Fe, is observed between NiO and Cr_2O_3 . It is likely that this oxide corresponds to the spinel phase identified by XRD analysis. In addition, Nb is also detected in locations of the oxide scale where Ni and Cr are also present. The Ni–Cr–Nb oxide should be a second spinel-type oxide that might coincide with the first spinel oxide on the XRD patterns.

At 650 °C, the domes formed at the outer part of the corrosion scale have a relatively porous NiO wall, in agreement with surface SEM–EDS and XRD analyses. The inner dense part is composed of a Ni–Cr spinel oxide that is richer in Cr toward the metallic substrate. Although low intensity peaks of Cr_2O_3 are identified after different short exposure times on XRD patterns, X-ray mappings and cross-section SEM–EDS analysis do not show a continuous Cr_2O_3 layer. Grains of this oxide are observed locally, but overall, the oxide scale mainly consists of a Cr-rich $(\text{Ni,Cr})_3\text{O}_4$ spinel. Through these analyses, a second spinel oxide containing Ni, Cr and Nb was also identified, as observed at 800 °C.

Finally, at both temperatures, X-ray mappings revealed a strong depletion of Cr in the metallic matrix beneath the oxide scale. The Cr content in the metal close to the interface with the oxide is much lower at 800 °C than at 650 °C, 5 wt.% versus 12.4 wt.%, respectively. These values do not evolve with time but the thickness of the Cr-depleted area is increasing with the exposure time as highlighted by Table 3. The Cr-depleted area thickness corresponds to the zone where the Cr content is below the nominal value in the alloy, 21.5 wt.% (value that is still found after aging beneath the depleted area and that remains constant all over the non-affected metallic substrate). It can be noticed that the depth of the damaged metal is much more important at 800 °C than at 650 °C.

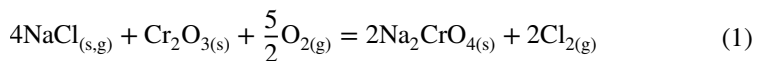
Table 3 Affected metal zone thickness (in μm) depending on temperature and exposure time

	24 h	100 h	500 h	1000 h	2500 h	5000 h
650 °C	–	3	4	6	8	8
800 °C	13	45	63	143	195	–

Discussion

In laboratory air, alloy 625 exhibits an excellent corrosion resistance at temperatures up to 1000 °C. Indeed, data present in the literature indicate that at these temperatures, alloy 625 forms a protective layer of Cr₂O₃ that grows following a parabolic law [5–7, 22, 23]. All the characterizations carried out on alloy 625 with solid NaCl deposit after various exposure times at 650 and 800 °C revealed thick corrosion scales, damaged by cracks, blisters, pores and spalling, and highly damaged subsurface areas (Figs. 1 and 2). In these exposure conditions, for both exposure temperatures, the corrosion scale is made of non-protective oxides. The catastrophic degradation of alloy 625 observed in this study is therefore due to the presence of NaCl and can be attributed to the active corrosion mechanism described in the literature [10–13] and detailed in a previous investigation for exposure at 800 °C [22]. However, even if at both temperatures the oxide scale is non-protective and heavily damaged, the characterizations performed in the present study indicate a strong effect of the temperature on the degradation mechanisms of the alloy 625. At 800 °C, oxide scales and affected subsurface metal zones are much thicker than at 650 °C. In addition, after exposure at 800 °C, the scale is mainly composed of a continuous thick layer of Cr₂O₃, which is not observed at 650 °C. In order to investigate these differences, the active corrosion mechanism at both temperatures needs to be addressed.

For solid NaCl deposit, the literature reports that the initiation of the active corrosion mechanism, for chromia-forming alloys, is based on the reaction between the native oxide Cr₂O₃, O₂ and gaseous NaCl, as described in Eq. 1 [11, 14, 19]. Indeed, for both temperatures, calculations of Gibbs free energy with FactSage® software provide negative values for reactions involving gaseous NaCl, whereas positive values are obtained considering solid NaCl. Results of calculations are given in Table 4.



The reaction given in Eq. 1 is initiating the active corrosion mechanism by releasing gaseous chlorine. Chlorine migrates to the metal substrate, where it reacts with the elements present in alloy 625. Figure 5 shows the evolution of Gibbs free energy of metal-chlorine reaction as a function of temperature, calculated with FactSage® software. Calculation results show that Nb and Cr chlorides are the most stable thermodynamically, while Ni and Mo chlorides are the least stable. However, it should be noted that these calculations were performed for pure elements, therefore for an activity equal to unity. As a consequence, the Gibbs free energy values might be different for alloy 625, where the activities of elements in solid solution are lower than 1. Nevertheless, the high Cr content in the corrosion products and the important Cr

Table 4 Gibbs free energy of reaction in Eq. 1 for solid or gaseous NaCl

	$\Delta G_{650^\circ\text{C}}$ (kJ)	$\Delta G_{800^\circ\text{C}}$ (kJ)
NaCl _(s)	169.8	182
NaCl _(g)	–195.3	–101.7

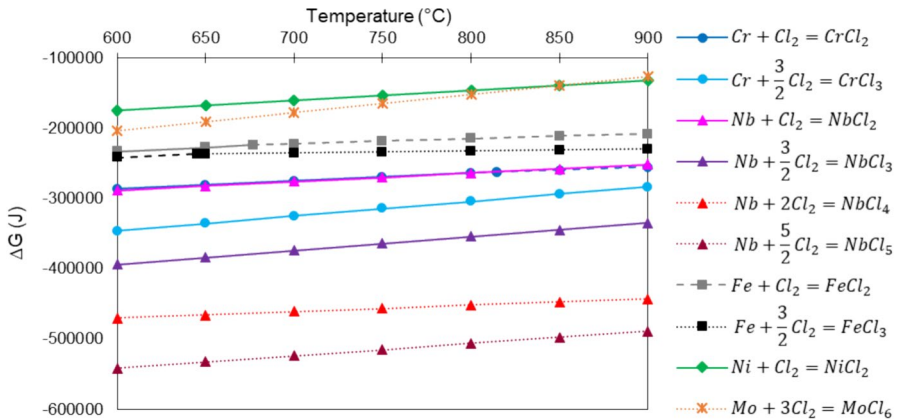
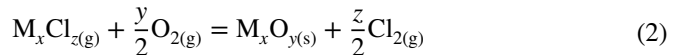


Fig. 5 Gibbs free energy for metal chloride formation from pure elements as a function of temperature (the state of metal chloride depends on temperature: solid line=solid, dashed line=liquid and dotted line=gaseous)

depletion in the subsurface matrix (Figs. 3 and 4) confirm that Cr is highly sensitive to chlorine attack at both temperatures, as suggested by results presented in Fig. 5.

The catastrophic degradation of the alloy caused by the active corrosion mechanism is partly due to the high volatility of metal chlorides at high temperatures. Once in gaseous state, metal chlorides migrate toward the external surface until reaching an oxygen partial pressure at which the oxide is thermodynamically more stable than the metal chloride. In consequence, the metal chloride transforms into the corresponding oxide, following the general equation:



The oxygen partial pressure required for the occurrence of each oxidation reaction explains the location of the different oxides in the corrosion products. The observations of the present work showed that NiO was found at the outer part of the corrosion scale, while Cr₂O₃ is found close to the substrate. Between NiO and Cr₂O₃, a Ni–Cr spinel oxide was also observed. Indeed, thermodynamic calculations done by X. Huang [24] showed that the Ni–Cr spinel forms from the reaction between NiO and Cr₂O₃ at temperatures higher than 400 °C. These results are in agreement with the findings of Zahs et al. [9] and are further discussed in previous investigations by Curnis et al. [22].

Figure 6 presents the evolution of saturation vapor pressures of the formed metal chlorides as a function of the temperature. Daniel et al. [25] reported that, above 10⁻⁴ bar, the evaporation of metal chlorides becomes highly critical and leads to the catastrophic degradation of the alloy. Figure 6 shows that, at 800 °C, the vapor pressures of all formed metal chlorides are close to or exceed 10⁻⁴ bar. Moreover, their gaseous transport in the metal is facilitated by the formation of the interconnected voids network, which is not present at lower temperature. At 650 °C, the vapor pressures, especially those of chromium chlorides which are among the

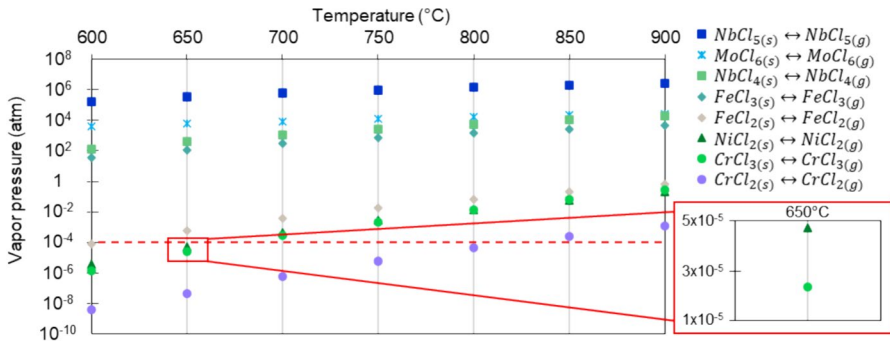


Fig. 6 Vapor pressure of metal chloride as a function of temperature

Table 5 Vapor pressure of Ni and Cr chlorides (atm)

Temperature (°C)	650	800
NiCl ₂	4.7 × 10 ⁻⁵	1.3 × 10 ⁻²
CrCl ₃	2.3 × 10 ⁻⁵	1.3 × 10 ⁻²

most easily formed, are still significant. Yet, they are 2 to 3 orders of magnitude lower than at 800 °C. It is therefore assumed that this lower volatility of chloride results in a slower kinetics of the phenomena involved in the active corrosion mechanism. As a consequence, the corrosion scales formed at lower temperatures are thinner and the thickness of the depleted matrix due to element consumption by metal chloride formation is less important. These results are in agreement with the observations of the present study.

In addition, the lower volatility of chlorides at 650 °C equally allows explaining the different compositions of the corrosion products observed at 650 and 800 °C. Indeed, even if the reaction between Ni and Cl₂ to form NiCl₂ is the least thermodynamically favored as compared to other elements present in the alloy 625, the vapor pressure of NiCl₂ is twice as high as the vapor pressure of CrCl₃ at 650 °C (the most favorable chromium chloride according to Fig. 5), while they are similar at 800 °C (Table 5). A higher vapor pressure for the chloride of the major constituent in the matrix strongly supported the idea of an increased participation of Ni in the active oxidation mechanism at 650 °C, as compared to what was observed at 800 °C. In addition, the lower volatility of chromium chlorides at 650 °C leads to the formation of isolated Cr₂O₃ grains, resulting from oxidation of CrCl₂/CrCl₃, which are in direct contact with NiO grains, resulting from oxidation of NiCl₂. As these two oxides cannot coexist [24], the spinel phase (Ni,Cr)₃O₄ is formed.

Another hypothesis proposed to explain the different corrosion scales composition is based on the microstructure of alloy 625. Indeed, a dendritic structure was observed in all as-built samples and it is due to Nb and Mo segregation during solidification, leading to an enrichment of these elements in the interdendritic regions. Observations of the unaffected matrix revealed that the dendritic substructure resulting from the LMD-*p* process was still present after

1000 h at 650 °C (Fig. 7a). This is in contrast with the observations performed on a sample aged 24 h at 800 °C where the chemical heterogeneity results in a microstructural heterogeneity with the precipitation of secondary phases containing Nb and located in the interdendritic regions (Fig. 7b). At 650 °C, Nb is more available to participate in the active corrosion mechanism than at 800 °C where Nb is trapped in the secondary phases. A higher concentration of Nb in the interdendritic zones might lead to a preferential attack of chlorine on Nb rather than on Cr. Indeed, Nb is the most sensitive to chlorine (Fig. 5) and forms gaseous chlorides (Fig. 6). This would further support the idea that less Cr chlorides would form, leading to less Cr₂O₃ formation, in agreement with SEM observations after 650 °C exposures.

Conclusions

The high-temperature behavior of alloy 625 elaborated by laser metal deposition-*powder* in the presence of NaCl solid deposit was investigated in the present study. The results showed that the presence of the deposit had catastrophic effect on the high-temperature oxidation behavior of alloy 625. This detrimental effect is more pronounced when the temperature increases from 650 to 800 °C. The active corrosion mechanism taking place in these exposure conditions leads to the formation of thick corrosion scales, made of different oxides and to the degradation of the metallic substrate. Differences between the phenomena that occurred at the two temperatures were highlighted in the present study. To explain the different behavior of alloy 625 exposed at 650 and 800 °C, in addition to the increase of kinetics related to the increase of temperature, a main factor appears to be the vapor pressure of different metallic chlorides. At 650 °C, Ni chlorides exhibit higher vapor pressure than Cr chlorides, while at 800 °C, their vapor pressures are similar. This result suggests that Ni chlorides are more prone to form and to migrate toward the surface at 650 °C, while at 800 °C, Cr chlorides are the main species to form and to participate in the growth of the oxide scale.

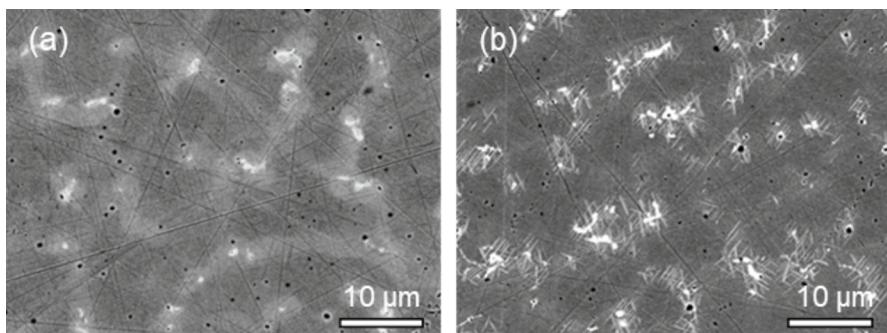


Fig. 7 SEM images of LMD-*p* alloy 625 after **a** 1000 h at 650 °C and **b** 24 h at 800 °C

Acknowledgements This work was financially supported by IRT Saint Exupéry. The authors would like to thank Frédéric Herbst and Nicolas Goeffroy from ICB laboratory for their technical support for SEM and XRD analyses.

Author Contribution A.C lead the investigation and wrote the main manuscript text. I.P and A.P wrote some parts of the text and reviewed the manuscript. J.M.B made calculations to prepare Figs. 5 and 6 and data presented in Tables 4 and 5. S.B reviewed the manuscript.

Data Availability No datasets were generated or analyzed during the current study.

Declarations

Conflict of interest The authors declare no competing interests.

References

1. D. Monceau and M. Vilasi, *JOM* **74**, 2022 (1659–1667).
2. C. Thomas and P. Tait, *International Journal of Pressure Vessels and Piping*. **59**, 1994 (41–49).
3. S. Floreen, G. Fuchs, and W. Yang, *Superalloys* **718**, 1994 (13–37).
4. L. E. Shoemaker, *Superalloys* **718**, 2005 (409–418).
5. N. Ramenatte, A. Vernouillet, M. Vilasi, D. Monceau, et al., *Corrosion Science* **164**, 2020 (108347).
6. M. Sharifitabar, S. Khorshahian, N. K. Jain, et al., *Corrosion Science* **197**, 2022 (110087).
7. D. M. England and A. V. Virkar, *Journal of the Electrochemical Society* **146**, 1999 (3196).
8. E. Schaal, Comportement en corrosion de matériaux métalliques commerciaux et modèles dans des conditions types UVEOM. Université de Lorraine (2015).
9. A. Zahs, M. Spiegel, and H. J. Grabke, *Corrosion Science* **42**, 2000 (1093–1122).
10. Y. Y. Lee and M. J. McNallan, *Metallurgical and Materials Transactions A* **18**, 1987 (1099–1107).
11. H. J. Grabke, E. Reese, and M. Spiegel, *Corrosion Science* **37**, 1995 (1023–1043).
12. M. Spiegel, A. Zahs, and H. J. Grabke, *Materials at High Temperatures* **20**, 2003 (153–159).
13. J. Phother-Simon, I. Hanif, T. Jonsson, and J. Liske, *Fuel* **357**, 2024 (130012).
14. N. Hiramatsu, Y. Uematsu, T. Tanaka, and M. Kinugasa, *Materials Science and Engineering: A* **120–121**, 1989 (319–328).
15. D. Fantozzi, V. Matikainen, P. Vuoristo, et al., *Surface and Coatings Technology* **318**, 2017 (233–243).
16. L. Chen, H. Lan, W. Zhang, et al., *Engineering Failure Analysis* **79**, 2017 (245–252).
17. Y. Kawahara, *Corrosion Science* **44**, 2002 (223–245).
18. F. J. Pérez, M. P. Hierro, and J. Nieto, *Materials and Corrosion* **59**, 2008 (566–572).
19. X. Wang, Z. Liu, K. Cheng, and Y. Kong, *Corrosion Science* **216**, 2023 (111102).
20. K. Wu, W. Sun, W. Zhou, et al., *Corrosion Science* **207**, 2022 (110536).
21. R. Bender and M. Schütze, *Materials and Corrosion* **54**, 2003 (652–686).
22. A. Curnis, I. Popa, A. Prillieux, J.-M. Brossard and S. Chevalier, *Corrosion Science* (2024).
23. A. Chyrkin, K. O. Gunduz, I. Fedorova, et al., *Corrosion Science* **205**, 2022 (110382).
24. X. Huang, Défauts ponctuels dans Cr₂O₃ et oxydation d'un alliage Ni-30Cr à haute température : approches expérimentale et numérique. Université Grenoble Alpes (2022).
25. P. L. Daniel and R. A. Rapp, Halogen Corrosion of Metals. in *Advances in Corrosion Science and Technology*, vol. 5, eds. M. G. Fontana and R. W. Staehle (Springer, US, Boston, 1976), pp. 55–172.

Publisher's Note Springer Nature remains neutral with regard to jurisdictional claims in published maps and institutional affiliations.

Springer Nature or its licensor (e.g. a society or other partner) holds exclusive rights to this article under a publishing agreement with the author(s) or other rightsholder(s); author self-archiving of the accepted manuscript version of this article is solely governed by the terms of such publishing agreement and applicable law.

Authors and Affiliations

Agathe Curnis^{1,2} · Ioana Popa² · Aurélien Prillieux¹ · Jean-Michel Brossard³ · Sébastien Chevalier²

✉ Aurélien Prillieux
aurelien.prillieux@irt-saintexupery.com

Agathe Curnis
agathe.curnis@irt-saintexupery.com

Ioana Popa
ioana.popa@u-bourgogne.fr

Jean-Michel Brossard
jean-michel.brossard@veolia.com

Sébastien Chevalier
sebastien.chevalier@u-bourgogne.fr

¹ IRT Saint Exupéry, 3 rue Tarfaya, 31405 Toulouse Cedex 4, France

² ICB, UMR 6303CNRS-Université de Bourgogne, 21078 Dijon Cedex, France

³ Veolia Recherche et Innovation, Zone portuaire de Limay, 291 avenue Dreyfous-Ducas, 78520 Limay, France